Laser plasma plume structure and dynamics in the ambient air: The early stage of expansion

M. Cirisan, J. M. Jouvard, L. Lavisse, L. Hallo, and R. Oltra

Related Articles

Surface processing technique based on opto-hydrodynamic phenomena occurring in laser-induced breakdown of a microdroplet
Appl. Phys. Lett. 100, 104104 (2012)

Production and acceleration of ion beams by laser ablation
Rev. Sci. Instrum. 83, 02B717 (2012)

Proton emission from a laser ion source
Rev. Sci. Instrum. 83, 02B310 (2012)

Optical diagnosis and theoretical simulation of laser induced lead plasma spectrum
Phys. Plasmas 19, 013302 (2012)

Saturation effects in femtosecond laser ablation of silicon-on-insulator
Appl. Phys. Lett. 99, 231108 (2011)

Additional information on J. Appl. Phys.

Journal Homepage: http://jap.aip.org/

Journal Information: http://jap.aip.org/about/about_the_journal

Top downloads: http://jap.aip.org/features/most_downloaded

Information for Authors: http://jap.aip.org/authors
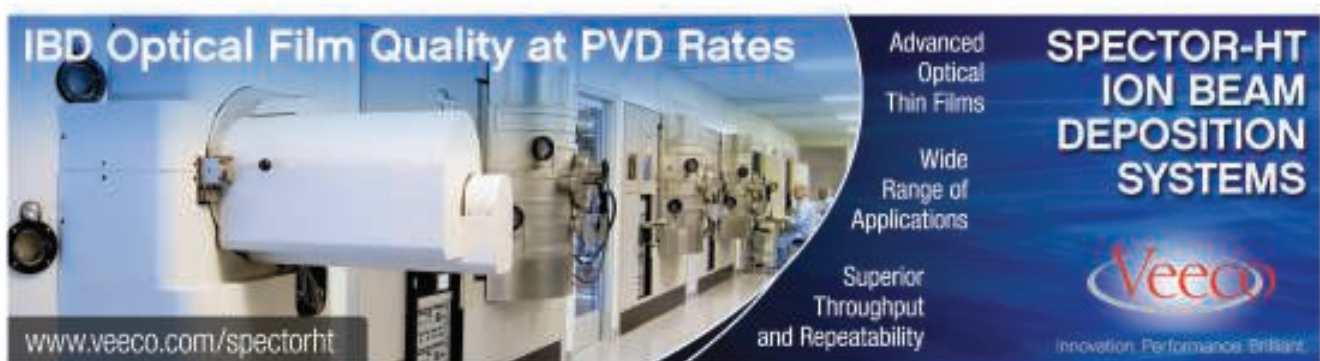
Laser plasma plume structure and dynamics in the ambient air: The early stage of expansion

M. Cirisan,[1] J. M. Jouvard,[1,a)] L. Lavisse,[1] L. Hallo,[2] and R. Oltra[3]

[1]*Laboratoire Interdisciplinaire Carnot de Bourgogne, UMR 5209 CNRS – Université de Bourgogne, 1 allée des Granges Forestier, F-71100 Chalon-Sur-Saône, France*
[2]*CELIA, UMR 5107 – Université Bordeaux 1, 351 cours de La Libération, 33405 Talence Cedex, France*
[3]*Laboratoire Interdisciplinaire Carnot de Bourgogne, UMR 5209 CNRS – Université de Bourgogne, 9 Avenue Alain Savary, F-21078 Dijon Cedex, France*

Laser ablation plasma plume expanding into the ambient atmosphere may be an efficient way to produce nanoparticles. From that reason it would be interesting to study the properties of these laser induced plasmas formed under conditions that are known to be favorable for nanoparticles production. In general, plume behavior can be described as a two-stage process: a "violent" plume expansion due to the absorption of the laser beam energy (during the laser pulse) followed by a fast adiabatic expansion in the ambient gas (after the end of the laser pulse). Plasma plume may last a few microseconds and may have densities 10^{-6} times lower than the solid densities at temperatures close to the ambient temperature. Expansion of the plasma plume induced by the impact of a nanosecond laser beam ($\lambda = 1064$ nm) on the surface of metallic samples in the open air has been investigated by means of fast photography. Spatio-temporal evolution of the plume at the early stage of its expansion (first 330 ns) has been recorded. Structure and dynamics of the plasma plume have been investigated and compared to numerical simulations obtained with a hydro-code, as well as some scaling laws. In addition, measurements using different sample materials (Al, Fe, and Ti) have been performed in order to analyze the influence of target material on plume expansion. © 2011 American Institute of Physics. [doi:10.1063/1.3581076]

I. INTRODUCTION

Laser ablation (LA) technique is nowadays largely used for both fundamental research and industrial applications. First of all, there is a variety of laser material processing procedures, like machining (marking, texturing…),[1–3] micromachining,[4–6] microstructuring,[7] etc. In addition, pulsed laser deposition (PLD)[8] is frequently used for the growth of thin films of classic[9,10] and new materials,[11,12] as well as for nanoparticles and clusters production.[13–15] There are also a few diagnostic techniques for chemical analysis based on LA, like laser induced plasma spectroscopy (LIPS)[16,17] and laser ablation inductively coupled plasma mass spectrometry (LA-ICP-MS).[18] Lately, with the development of high power ns to ps lasers, LA finds more and more applications in surgery.[19–22] For a further development of laser ablation based technologies, it is necessary to better understand the phenomena occurring during the laser – matter interaction.

The impact of a short and intense laser pulse on the surface of treated material induces a material removal and formation of a plasma plume above the sample surface. The plume containing particles of the ablated matter expands with a supersonic velocity in the surrounding atmosphere. Dynamics of this plasma plume strongly influence the processes occurring at the surface of the treated material. The process of LA, including the formation and expansion of the plasma plume, has been investigated both experimentally and theoretically for the last two decades. Even though a lot of efforts

have been made, this phenomenon is not yet completely understood. This is due to the fact that the process of LA is very complex, including a number of physical processes like heat transfer, material melting and evaporation, formation and expansion of the plasma plume, plasma – laser beam interaction, shock waves formation and propagation, plasma radiation, etc. All these processes occur more or less simultaneously and influence each other.

In case of metals as oxydable as titanium,[23] formation of the plasma plume during the LA in the open air induces a specific reactivity, i.e., it allows insertion of nitrogen and oxygen atoms into the sample surface. During its expansion in the air, this high pressure plasma enhances the formation of aggregates. The size and the structure of these particles strongly depend on processing parameters, in particular laser fluency and pulse frequency.[24] Under certain conditions, nanoparticles can be generated. This nanopowder is formed in the plasma plume and then deposited on the target surface around the interaction zone.[24] Formation of nanoparticles has been observed in case of titanium, as well as others metals like iron[25] and aluminum.[26]

Study of the interface ablated matter – air, where the shock wave is generated, is very important. In this area, the pressure is higher, so the reactions of metal atoms with oxygen or nitrogen atoms from the air can be enhanced via thermodynamical equilibrium (saturation) and nonequilibrium (condensation) mechanisms, leading to the matter condensation.

Fast photography is a technique frequently used for studying the expansion of the laser ablation plume in vacuum or in a low pressure ambient gas. This technique allows one

a)Electronic mail: jean-marie.jouvard@u-bourgogne.fr.

109, 103301-1

to probe a large plasma region. Fast photography detects plasma radiation, being a function of particles densities and temperature. Harilal *et al.*[27,28] used this technique to investigate the expansion dynamics of the plasma generated during ns laser ablation of Al target in air at low background pressures. They have observed effects like plasma plume splitting and sharpening. Gurlui *et al.*[29] presented a detailed temporal evolution of aluminum plasma induced by ns laser in vacuum. Amoruso *et al.*[30] examined dynamics of laser ablation plume of manganates in low pressure oxygen atmosphere.

Still, one should keep in mind that behavior of plasma plume induced in vacuum or at low background pressure significantly differs from the behavior of plasma plume induced at atmospheric pressure. The interaction of the plasma plume with the background gas is a very complex physical process involving effects like plume deceleration, shock waves formation, attenuation, diffusion, reactive scattering, plume thermalization.[28] As a consequence, the plasma plume gets spatially confined. In that case, the plume size is much smaller, so one is obliged to use a macro objective in order to visualize the plume. Barthelemy *et al.*[31] employed fast photography to examine expansion geometry of the plasma plume induced by UV ns laser pulse on Al target in the open air. Wu *et al.*[32] used this technique to investigate the early stage of aluminum plasma expansion in order to verify their numerical model. In this work,[32] ablation was performed in the open air using a ns laser emitting at 532 nm, but only a few experimental points are given. Other authors recorded expanding plasma plume induced by ns laser impact on materials like silicon crystal[33] and iron oxide.[34]

In this work, we have employed fast photography technique to investigate dynamics of the plasma plume induced by the impact of near IR ns laser beam on metallic samples in the open air. Series of images showing spatio-temporal evolution of the plasma plume during the first 330 ns of the plasma life have been recorded. A structure of the plasma plume has been observed. Two plume regions have been distinguished — *plume core* and *plume periphery*. Temporal evolutions of the plume core and periphery dimensions (diameter and length) have been analyzed and compared to numerical simulations. Plume core and periphery expansion velocities have been determined. A discussion regarding the effect of ambient pressure on plasma plume expansion is given. In addition, influence of the laser beam irradiance and the target material on the plasma plume dynamics has been investigated. Measurements performed using different sample materials (Al, Fe, and Ti) allow one to estimate which one of these metals is more appropriate for nuclei formation in the expanding plasma plume.

This is the first part of the work dedicated to powder generation. Here, we focus on plasma generation and our main interest is the diagnostics of plasma plume thermodynamic conditions. A simulation of plasma thermodynamics should complete the results of this work by studying saturation and condensation processes in the plasma plume during its hydrodynamic expansion using a hydro-code and models developed at CELIA and CESTA.[25] This analysis will give a better understanding of the mechanisms involved in the formation of nanoparticles present in the plume.

Section II gives a description of the experimental setup and measurements performed in this work. Experimental results are presented and discussed in Sec. III. In Sec. IV, we give some estimates obtained from models and present the results of numerical simulations, which are then compared to the obtained experimental results.

II. EXPERIMENTAL SETUP

A schematic representation of the experimental setup used in this work is shown in Fig. 1.

Laser ablation was performed by a Nd:YAG laser (Quantel Brilliant b) emitting 5.1 ns laser pulses at 1064 nm with repetition rate of 10 Hz. Maximal energy per pulse is 0.974 J. Unfocused laser beam has a Gaussian intensity distribution. Laser beam was directed perpendicularly to the sample surface. The beam was focused onto the sample surface using a 1 m focal length lens. The laser spot diameter was 1.72 mm. In this experiment, only the average laser beam irradiance was determined. The laser beam fluency was measured by a powermeter and the area of the laser impact spot on both thermal paper and metallic sample using a microscope. The average laser beam irradiance was varied between 2.74 and 8.16 GW/cm^2. The indicated values of laser irradiance correspond to the incident laser beam. Ablation was performed on samples of commercially pure Al, Ti (CP4), and Fe (Armco). The sample surface was cleaned, but not polished in order to avoid high reflectance of the used metallic material to the laser beam radiation. The metallic sample surface becomes stable very quickly, after only a few laser impacts. This is due to the fact that the surface roughness does not evolve much for the laser fluencies considered in this work.[35] All experiments were performed in air at the atmospheric pressure.

An ICCD camera (Andor Technology) equipped by a macro objective (Computar) was used for recording the plasma plume images at different instants of the plasma life. By adjusting the objective's focal length and adding extension
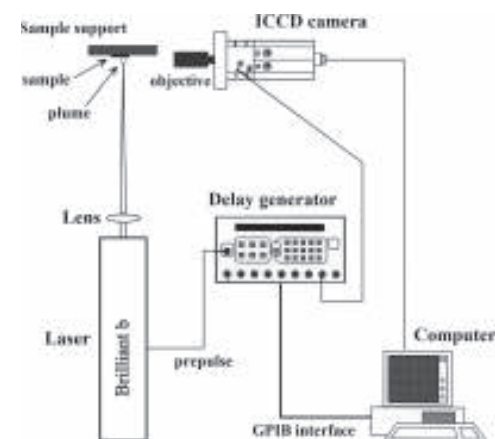
FIG. 1. Experimental setup.

tubes, magnification of 1:1.066 was achieved. This means that the image of the plasma plume on the ICCD camera matrix (1024×256 pixels, 1 pixel $= 26$ μm $\times 26$ μm) is slightly larger than its real size. The ICCD camera was detecting plasma radiation in the visible wavelength range (350–850 nm). The gate width was set to 5.4 ns, whereas gate delay between the instants at which plume images were taken was set to 10 ns. A delay generator was used to synchronize the ICCD camera with the laser, as well as to generate time delays. One hundred fifty ns before emitting the laser beam, laser was sending a TTL signal to delay generator, which then triggered the ICCD camera, that way setting it up ready for acquisition. A computer was used for controlling the experimental system, as well as for data acquisition.

Imaging was performed perpendicularly to the laser beam direction, so the obtained images show a side view of the expanding plasma plume, with the sample being positioned vertically on the right side of the image. In order to reduce the reflection of light from the sample surface captured by the camera, laser impacts were performed close to the sample edge.

Having a laser working in pulsed regime with repetition rate of 10 Hz, series of images showing the spatio-temporal evolution of plasma plume were recorded. Every image in a series corresponds to a different laser pulse. It was observed that after first 10 to 15 pulses plasma plume gets quite reproducible, so all recordings were performed after this initial period. A fresh sample surface was used for recording each new series of images. For recording one series of images, less than 100 shots were performed at the same spot of the sample surface. Under the experimental conditions in this work, the ablation depth is of the order of nm, so even after 100 shots the depth of the ablated material is still less than 1 μm.

Each recorded image represents a spatial distribution (2D) of the radiation emitted by the plasma plume at a given instant. In case of dense plasmas, whose electron density is larger than the critical density, thermal emission corresponds to the radiative emission of an optically thick plasma. Under the experimental conditions in this work, the expanding plasma plume (few mm in size) is expected to have an electron density lower than the critical one. In that case, plasma radiation is generated by free – free transitions (bremsstrahlung radiation), free – bound transitions (recombination radiation) and bound – bound transitions (spectral lines radiation). Bremsstrahlung radiation is expected to bring the main contribution to the plasma plume radiative emission.

The images recorded by the ICCD camera correspond to the hot zones of the laser ablation plume, where temperatures and particle densities are sufficiently high leading to intensive plasma radiation. Study of these hot zones of the plume is of particular interest for understanding the process of nanoparticles formation. Indeed, powder is expected to be generated during the adiabatic expansion of the plasma plume into the ambient atmosphere. In the next section, the hot zones of the laser ablation plume will be referred as "the plasma plume."

III. EXPERIMENTAL RESULTS

A. Plasma plume structure

A series of images showing spatio-temporal evolution of plasma plume at the early stage of its expansion is given in Fig. 2. Laser ablation was performed on aluminum sample, using the laser beam intensity of 8.16 GW/cm^2. Aluminum samples were used for these measurements, since the plasma plume was stable and reproducible even when using the
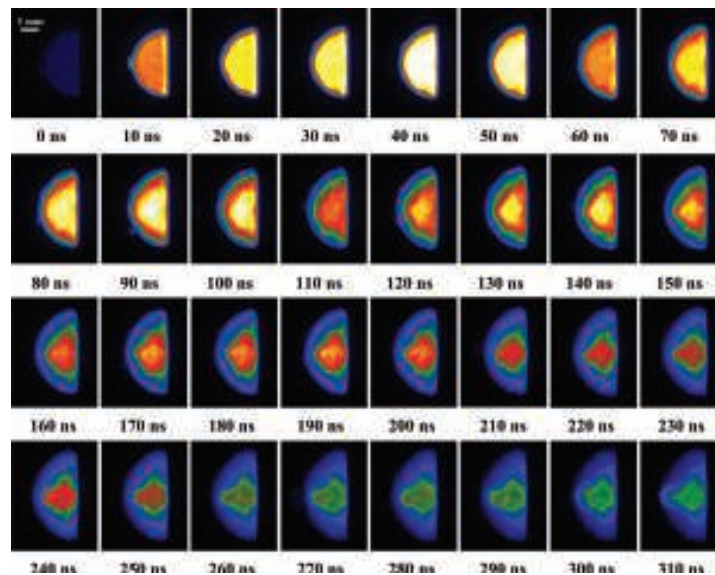
FIG. 2. (Color online) A series of images showing spatio-temporal evolution of the plasma plume.
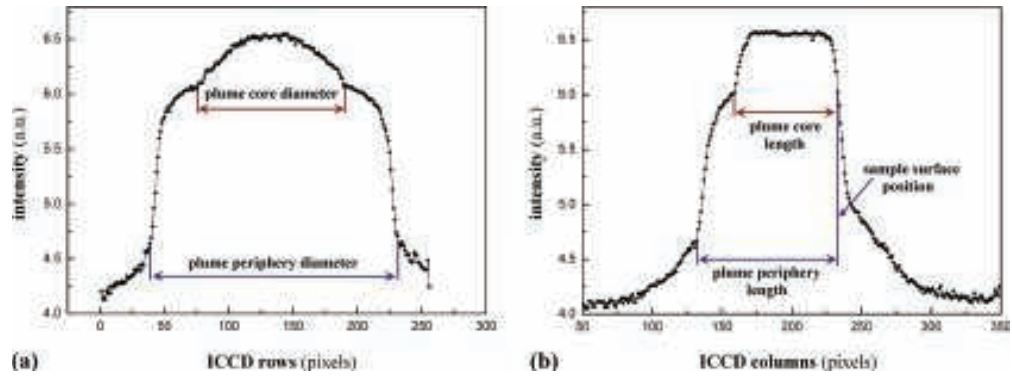
FIG. 3. (Color online) Examples of the plume radiation intensity distribution along the plume's (a) diameter and (b) axis of symmetry.

highest beam intensity provided by the laser. Under these conditions, the plasma life lasts for about several microseconds, but recordings were performed only during the first 330 ns. Instants of plasma life at which the images were taken are indicated below the images. The real dimensions of each image in the series are 4.34 mm × 5.51 mm.

Colors in the images indicate different radiation intensity values. White color corresponds to the maximal and black to the minimal radiation intensity. Attention was paid to avoiding the ICCD camera pixels saturation. The color scale was fixed during the recording of the entire series of images.

The first image (see Fig. 2 − instant 0 ns) can be considered as the moment of plume formation. One should keep in mind that the gate width was 5.4 ns, representing the incertitude of the indicated instant of the plasma life. Low radiation intensity might mean that the plume actually formed between 0 ns and 5.4 ns.

As it can be seen from Fig. 2, the hot plasma plume shape is clearly hemispherical, as previously observed in Barthelemy *et al.*,[31] and the plume expands both longitudi-

nally and radially with the time. One should keep in mind that the Gaussian intensity distribution of the laser beam most likely contributes to the shape of the plasma plume.

When analyzing the plume structure, at a first glance, one can observe the central, most radiant part of the plume and the surrounding, less radiant area. At this moment, one cannot tell if there are two regions of the hot plasma plume or there is simply a gradual decrease of the radiation intensity from the center to the periphery of the plume. In order to have a better insight in plume radiation intensity distribution, instead of analyzing the images, one should analyze the signals obtained directly from the ICCD camera.

Examples of signals showing the distribution of plume radiation along the plume's diameter and axis of symmetry are given in Fig. 3. For a better comprehension, an illustration is given in Fig. 4. The plume's axis of symmetry corresponds to the direction of the laser beam. Now, by observing the signals (Fig. 3), one can clearly see the structure of the plasma plume. In both Figs. 3(a) and 3(b), one can easily distinguish two plasma plume regions. We shall call them *plume core* and *plume periphery*. The core is the central,
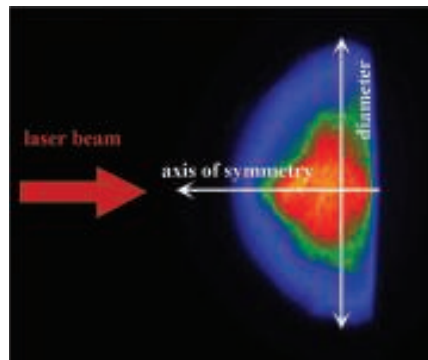
FIG. 4. (Color online) Illustration: plasma plume diameter and axis of symmetry. Image recorded at 200 ns; plume diameter: 4.62 mm; plume length: 2.44 mm.
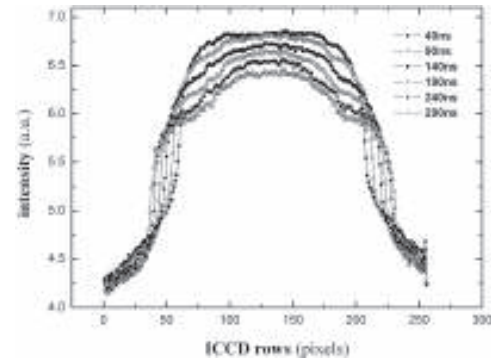
FIG. 5. Plume radiation intensity distribution along the plume diameter at different instants of the plasma life.
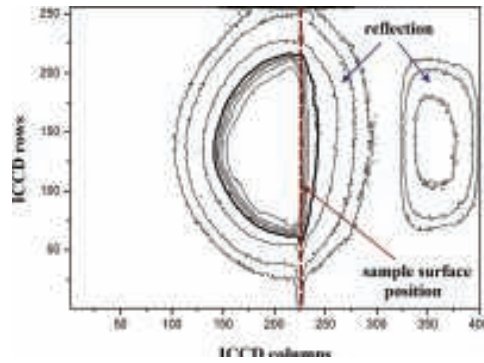
FIG. 6. (Color online) Determination of the sample surface position: dashed line – position of the sample surface; thick contour – plume periphery edge. Image recorded at 30 ns.

most radiant part of the plasma plume; whereas periphery is the surrounding, less radiant area.

Two concentric hemispherical plume regions, having different refractive indexes, have been also observed in Hauer *et al.*[36] using interference shadowgraphy. Even though experimental conditions (laser wavelength, pulse energy, material) in this work were different from ours and shadowgraphy images were taken at later instants, the structures of the expanding plasma plumes are very similar. Furthermore, two hemispherical plume regions corresponding to higher electron densities have been observed using a two-wavelength interferometry in Schittenhelm *et al.*[37] In addition, side view photographies of the expanding Al plasma plume in Barthelemy *et al.*,[31] recorded with and without band-pass filters (corresponding to the most intense Al I and Al II line), indicate that dimensions of the ablated matter plume are smaller than the ones of the integral plasma plume. This, in addition to our results, confirms the existence of the plasma plume structure.

The apparent reduction of the central part of the plume with the time, observable in the images (Fig. 2), is due to the radiation intensity decrease. This can be clearly seen in Fig. 5, showing the plume radiation distribution along the plume diameter at different instants of the plasma life. Here, one can notice that distinction between the plume core and plume periphery becomes more pronounced with the time. Furthermore, it can be observed that both plume core and periphery diameter increase with the time, even though the increase of the core diameter is less noticeable than the one of the periphery. On the other hand, due to the plume radiation intensity decrease, the part of the plume characterized by radiation intensity over a certain value, corresponding to a certain color in the image, reduces. This is the reason of the apparent reduction of the central part of the plume with the time, observed in the images (Fig. 2). In fact, the plume core diameter increases with the time, as observed from signals provided directly by the ICCD camera (Fig. 5).

Plume core and periphery dimensions i.e. diameter and length can be measured as shown in Fig. 3. The edges of both core and periphery can be easily determined. Measurements along the plume diameter were performed at a certain distance from the sample surface, where the plume diameter was estimated to be the largest. As it can be seen from Figs. 4 and 6, the plume diameter was not the largest at the sample surface, but at a certain distance above it. Position of the sample surface was determined as shown in Fig. 6. Every contour in Fig. 6 corresponds to a different radiation intensity value. The highest radiation intensity values, corresponding to the central part of the plume, were excluded from the image in order to have a better insight in the radiation distribution at the plume edges. The thick contour represents the plume periphery edge. Contours outside the plume periphery edge correspond to very low radiation intensities. Distortions of low intensity contours on both sides of the plume are the indicators of sample surface position. The straight dashed line represents the position of the sample surface. Low intensity radiation on the right side of the straight dashed line corresponds to the light reflected from the Al sample surface and captured by the objective.
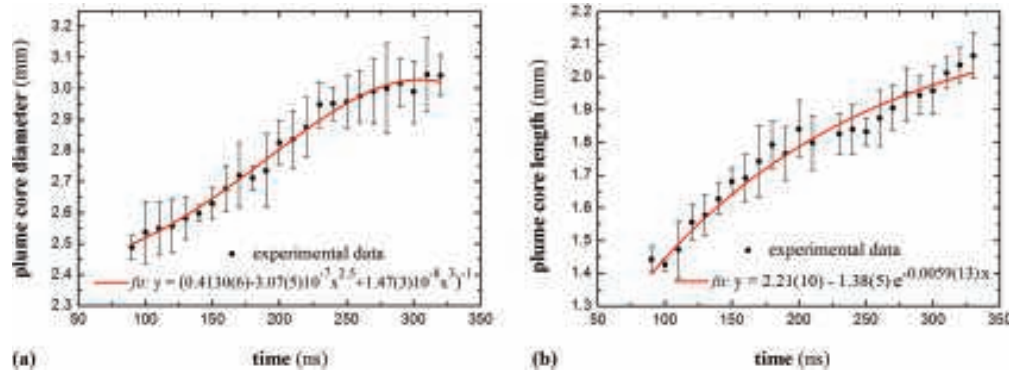
FIG. 7. (Color online) Temporal evolution of plume core (a) diameter and (b) length.
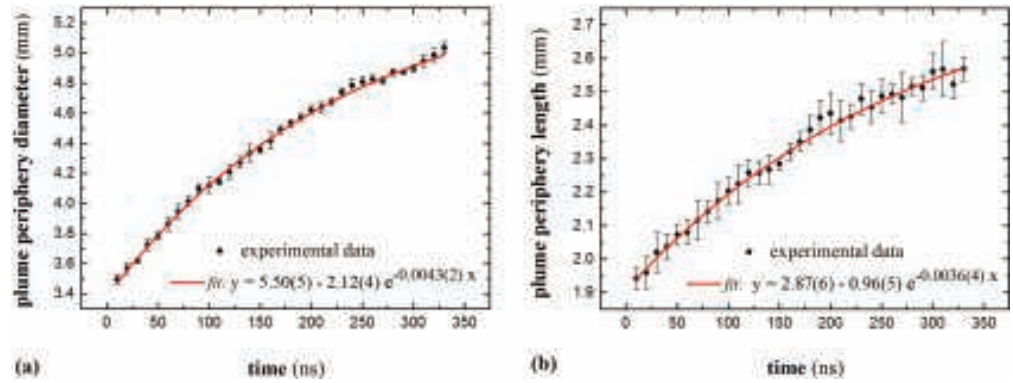
FIG. 8. (Color online) Temporal evolution of plume periphery (a) diameter and (b) length.

A possible explanation of the plasma plume structure i.e. the existence of two plume regions can be given in the following manner:

• *Plume core* is the central part of the plasma plume, predominantly containing heated and ionized ablated matter. Hence, the edges of the plume core should correspond to the ablated matter – air interface.
• *Plume periphery* at the lateral edges of the plume corresponds predominantly to the heated and ionized surrounding air.

This is in agreement with the spectroscopic observations of the plume induced under similar experimental conditions by De Giacomo *et al.*,[38] showing that nitrogen and oxygen atoms from the air are pushed ahead in front of the expanding ablated matter plume, containing atoms, and ions of the treated material. Still, one should keep in mind that the ablated matter – air interface is not so strictly defined, due to the intense interpenetration of ablated matter and surrounding air during the plume expansion, which gets even more pronounced at later times.

B. Plasma plume dynamics

In order to investigate the dynamics of the two plasma plume regions, temporal evolutions of the plume core and periphery diameter and length have been analyzed. Measurements of plume core and periphery dimensions were performed as shown in Fig. 3 for every recorded instant of the plasma life. The results are presented in Figs. 7 and 8. Each experimental point was obtained as a mean value of 10 measurements, and its uncertainty as the corresponding standard deviation. Curves in the graphs represent the best fitting functions and their analytical expressions are given in the corner of each figure.

As it can be seen from Figs. 7 and 8, dimensions of both plume regions are of the order of few millimeters. Furthermore, it is obvious that both plume core and periphery perform decelerated expansions in both radial and longitudinal direction, described in most cases by exponential functions.

Higher uncertainties in case of core dimensions (Fig. 7) are due to the more emphasized fluctuations at the edges of the plume core. There are also missing experimental points for the first 80 ns of the plasma life in Fig. 7, since it was not possible to distinguish core from periphery at these instants. Plume length of the order of millimeter at 10 ns of the plasma life [Fig. 8(b)] indicates the existence of a very "violent" plume expansion regime during the laser pulse duration ($\tau = 5.1$ ns).

By differentiating the functions fitted to the experimental data showing temporal dependences of the plume core and periphery radius and length, radial and longitudinal expansion velocities of both plume regions have been determined. Temporal evolutions of the plume core and periphery expansion velocities are given in Fig. 9. It can be seen that expansion velocities of the two plume regions are of the order of few thousands meters per second (supersonic velocities). These results are of the same order of magnitude as the values obtained by spectroscopic measurements of other
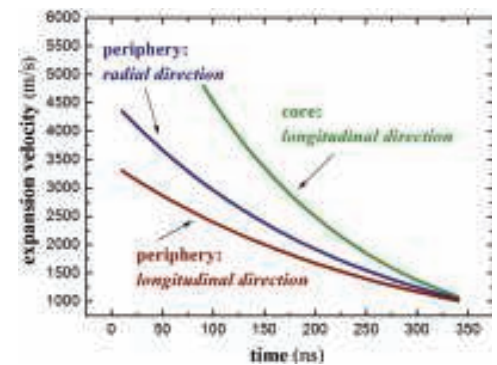
FIG. 9. (Color online) Expansion velocity of the plume core in the longitudinal direction (estimated error <25%) and expansion velocities of the plume periphery in the radial (estimated error <7%) and longitudinal direction (estimated error <16%).
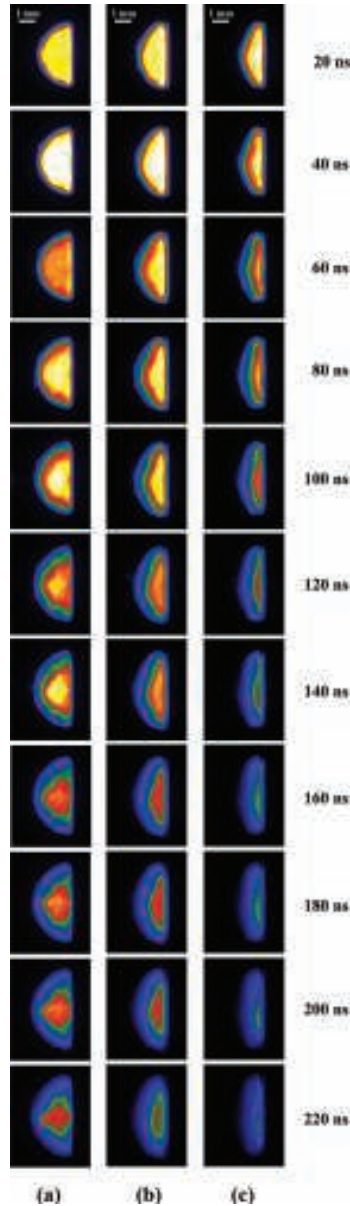
FIG. 10. (Color online) Spatio-temporal evolution of plasma plume induced by (a) 8.16 GW/cm^2, (b) 4.73 GW/cm^2 and (c) 2.74 GW/cm^2 intensity laser beam.

authors.[39,40] The plume expansion velocities presented in Fig. 9 manifest exponential decay temporal dependence. Reasons for this significant deceleration of plasma plume expansion will be discussed later. Here, we shall only men-

tion that this physical process corresponds to the expansion of a supersonic gas flow into a medium at rest. From Fig. 9, it can be clearly seen that the plume core expands with the highest velocity.

As we mentioned before, the images recorded by the ICCD camera in this work correspond to the hot zones of the laser ablation plume. So, one should keep in mind that these expansion velocities correspond to the hot plasma regions, which expand much slower than the plume edge. As seen, hot zones of the laser ablation plume expand with velocities of the order of 10^3 m/s. On the other hand, cold zones of the plume, which do not emit or emit very little radiation comparing to the hot zones, may expand with even higher velocities, as it will be shown later.

C. Influence of laser beam irradiance on plasma plume dynamics

In order to examine the influence of laser beam irradiance on plasma plume expansion, additional series of images have been recorded. Laser ablation was still performed on aluminum samples, but now different laser beam irradiance values have been employed: 8.16, 4.73, and 2.74 GW/cm^2. Laser beam irradiance was varied by changing the value of the laser beam energy per pulse. In Fig. 10, three series showing the spatio-temporal evolution of the plasma plumes corresponding to laser beam irradiances of 8.16, 4.73, and 2.74 GW/cm^2 are presented. In this figure, plasma plume spatio-temporal evolution is given with a step of 20 ns, but the measurements were performed with a step of 10 ns.

From Fig. 10, it can be clearly seen that plasma life lasts longer in case of higher laser beam intensities, due to the higher energy delivered by the laser pulse. On the other hand, one can notice a significant difference in shape of the plasma plumes induced by laser beams of different intensities. In case of 8.16 GW/cm^2 irradiance [Fig. 10(a)], plasma plume has a hemispherical shape. On the contrary, in case of lower irradiances (4.73 and 2.74 GW/cm^2), plasma plumes are much flatter [Fig. 10(b) and Fig. 10(c), respectively].

In order to examine the influence of laser beam irradiance on plasma plume expansion in more detail, temporal evolutions of the plume dimensions for different laser beam irradiances have been compared. In Fig. 11, temporal evolutions of both plume core and plume periphery diameter and length for different laser beam irradiance values are presented. It can be clearly seen that diameter of the plume core is larger in case of lower laser beam irradiance [Fig. 11(a)]. This might be related to the change of the laser beam intensity distribution due to the modification of the pulse energy. In this graph, experimental data for 2.74 GW/cm^2 irradiance are missing, since in this case it was not possible to distinguish plume core from plume periphery along the plume diameter. On the other hand, plume core length increases with the laser beam irradiance [Fig. 11(b)]. Here, one can notice different temporal evolutions of plume core length for different laser beam irradiance values. In case of the highest irradiance (8.16 GW/cm^2), the plume core length temporal evolution follows an exponential function. On the contrary, for the two lower irradiances (4.73 and 2.74 GW/cm^2), the plume core length is nearly constant,
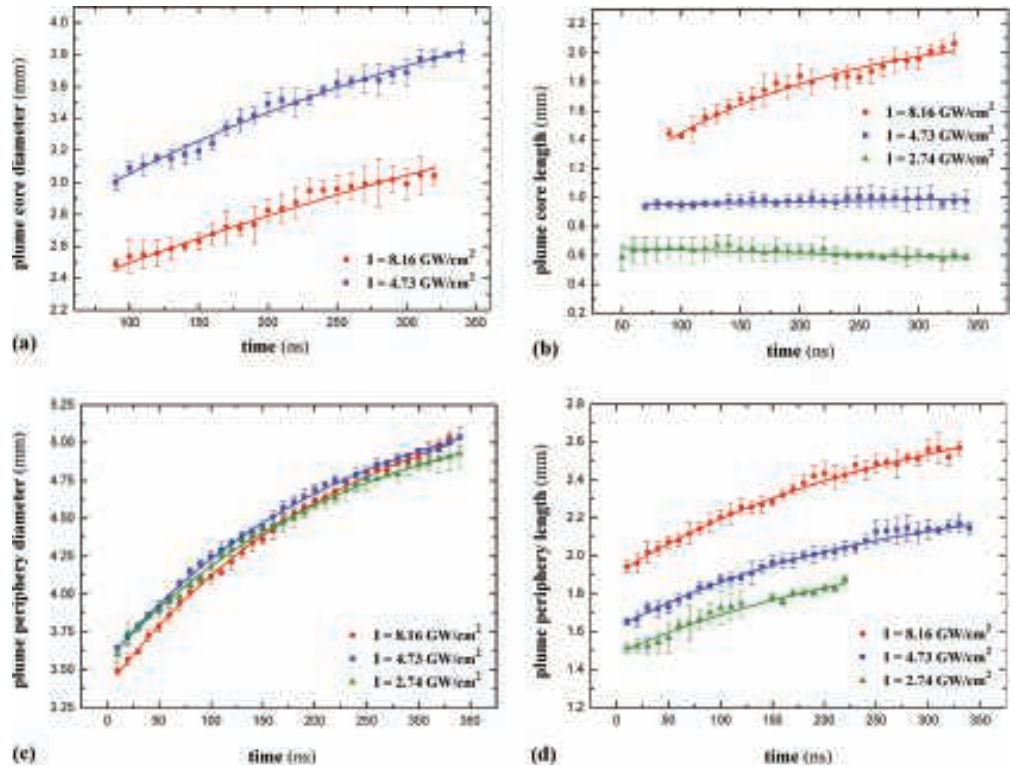
FIG. 11. (Color online) Temporal evolution of (a) plume core diameter, (b) plume core length, (c) plume periphery diameter and (d) plume periphery length for different values of laser beam intensity.

meaning that the plume core has reached its expansion limit. The stopping of the plume expansion has been previously observed by Aguilera *et al.*[41]

Plume periphery diameter values are very similar for all used laser beam irradiances [Fig. 11(c)]. On the other hand, plume periphery length increases with the laser beam irradiance [Fig. 11(d)]. Temporal evolutions of both plume periphery dimensions follow exponential functions for all used laser beam irradiances. Here, it can be noticed that for 4.73 and 2.74 GW/cm^2 irradiance values even though plume core has reached its expansion limit, the plume periphery continues its expansion in the longitudinal direction.

A higher irradiance laser beam delivers more energy to the target surface, as well as to the plasma plume formed above it. Higher temperature at the target surface leads to increased material evaporation rate, thus increasing the quantity of the ablated matter. At the same time, the plasma plume absorbs a larger quantity of laser radiation, thus increasing its internal energy. After the end of the laser pulse, the plume containing more ablated matter and having higher internal energy is capable of pushing the surrounding air far enough in front of itself in order to expand into a hemispherical shape. In case of lower laser beam irradiances, the ablation plume has less energy, so its expansion limit is reached much closer to the sample surface. In this case, the expansion in the radial direction prevails over the one in the longitudinal direction, so the plume core remains "attached" to the sample surface, having a more disklike shape (Fig. 10).

This significant change in the plume core behavior, particularly the one of the plume core length [Fig. 11(b)], with the increase of laser beam irradiance might also originate from different absorption wave mechanisms. Conesa *et al.*[42] suggested that transition from laser-supported detonation wave (LSDW) to laser-supported radiation wave (LSRW) regime occurs at 4.8 GW/cm^2. According to this, in case of 2.74 and 4.73 GW/cm^2 irradiance values, the LSDW would be responsible for plume expansion during the laser pulse duration; whereas in case of 8.16 GW/cm^2 irradiance, it would be the LSRW. This might also be the explanation of our results [Fig. 11(b)]. Above the 4.8 GW/cm^2 irradiance, plume expansion is more "violent" and propagates with a significantly higher velocity than at lower irradiances,[43,44] which can lead to such different fluid dynamics expansions after the end of the laser pulse.
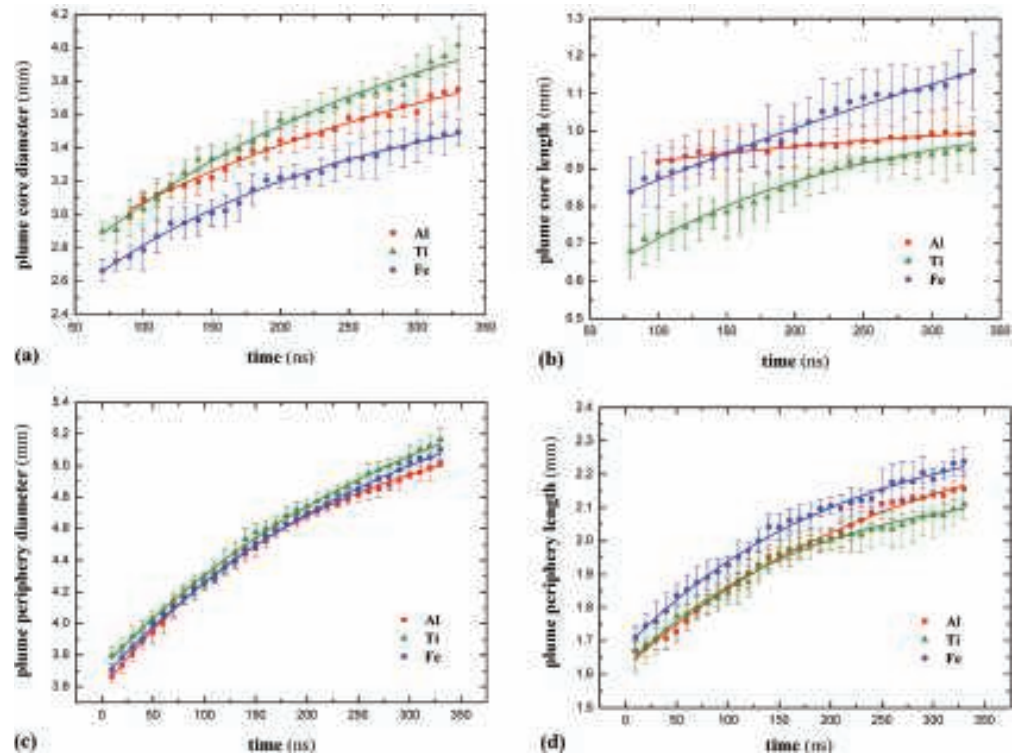
FIG. 12. (Color online) Temporal evolution of (a) plume core diameter, (b) plume core length, (c) plume periphery diameter and (d) plume periphery length obtained by laser ablation of Al, Ti, and Fe targets.

D. Influence of target material on plasma plume dynamics

In order to investigate the influence of target composition on plasma plume expansion, additional measurements using different metallic samples have been performed. In this experiment, samples of commercially pure Al, Ti, and Fe were used. These materials were chosen due to their frequent application in the industry, as well as their different physical properties, like atomic mass, thermal conductivity, latent heat of vaporization, etc.[45–48]

Laser ablation of Al, Ti, and Fe samples was performed using the laser beam irradiance of $I = 4.73$ GW/cm^2. The obtained results, i.e., temporal evolutions of the plume core and periphery dimensions for Al, Ti, and Fe samples are presented in Fig. 12. Each experimental point has been obtained as a mean value of 10 measurements, and its uncertainty as the corresponding standard deviation. Curves in the graphs represent the best fitting functions.

From Fig. 12, it is evident that target composition influences the behavior of the plasma plume. First of all, it can be noticed that the differences in plume dimensions are more emphasized in case of the plume core. For example, differen-

ces among the obtained periphery diameter or periphery length values for the used materials are lower than 6% [see Figs. 12(c), 12(d)]. On the other hand, the values of core diameter or core length of Al, Ti, and Fe plume differ for up to 20% [see Figs. 12(a), 12(b)]. This could be explained by the assumption previously made in Sec. III A. The behavior of the plume core, which predominantly contains the ablated matter, is much more influenced by the target composition than the one of the plume periphery, which corresponds to the heated and ionized surrounding air.

When observing the obtained results, one can notice that the values of plume periphery diameter are very similar for all used sample materials [Fig. 12(c)], whereas there is a significant difference between the plume core diameter values [Fig. 12(a)]. The core of Ti plasma has the largest diameter, whereas the core of Fe plasma has the smallest one. On the other hand, when analyzing the plume core and periphery length [Figs. 12(b) and 12(d)] one can see that Fe plasma is the one that reaches the furthest distance from the sample surface, whereas Ti plasma has the shortest length. To resume, Fe plasma gets more "detached" from the sample surface, whereas the Ti one remains more "attached" to it.

In addition, one could notice that temporal evolutions of Ti and Fe plume dimensions are relatively similar, but there is a certain discrepancy between their values. Here, one should compare the physical properties of Ti and Fe.[45–48] At a first glance, one would say that Ti and Fe are very similar metals. Still, thermal diffusivity of Fe ($d_{Fe} = 2.26 \times 10^{-5}$ m^2/s) is higher than the one of Ti ($d_{Ti} = 0.714 \times 10^{-5}$ m^2/s), meaning that the heat delivered by the laser pulse is faster transferred into the sample. On the other hand, the melting and boiling point, as well as the latent heat of fusion and particularly vaporization of Fe ($T_m = 1811$ K, $T_b = 3134$ K, $L_f = 2.47 \times 10^5$ J/kg, $L_v = 6.09 \times 10^6$ J/kg) are lower than the ones of Ti ($T_m = 1941$ K, $T_b = 3560$ K, $L_f = 3.05 \times 10^5$ J/kg, $L_v = 8.89 \times 10^6$ J/kg). Eventually, this might lead to a larger quantity of Fe vapor. In addition, atomic mass, which is slightly different in case of Ti ($M_{Ti} = 47.9$ g/mol) and Fe ($M_{Fe} = 55.8$ g/mol), plays a significant role in the fast adiabatic expansion of the plume.

Regarding Al plume, its dimensions do not differ that much from the ones of Fe and Ti plume. Still, there is a certain difference concerning its temporal evolution functions, particularly the one of the plume core length [Fig. 12(b)]. Al plasma plume core seems to have more-less reached its expansion limit in the longitudinal direction, i.e., its expansion is extremely slowed down. On the other hand, Fe and Ti plume, even though manifesting expansion deceleration, are still far from their expansion limits. Here, one should take into account that physical properties of Al are very different from the ones of Ti or Fe.[45–48] First of all, Al ($\alpha_{Al} = 0.2$) sample absorbs less laser radiation comparing to Ti ($\alpha_{Ti} = 0.45$) and Fe ($\alpha_{Fe} = 0.36$). Furthermore, thermal diffusivity of Al ($d_{Al} = 9.39 \times 10^{-5}$ m^2/s) is significantly higher than the ones of Ti and Fe, leading to a much faster heat transfer into the sample and a slower surface temperature increase. Then, even though the melting and boiling point of Al are lower ($T_m = 933$ K, $T_b = 2767$ K), there is still needed a lot of energy for fusion and evaporation process ($L_f = 3.97 \times 10^5$ J/kg, $L_v = 1.08 \times 10^7$ J/kg). And finally, there is a very significant difference between the atomic (molar) mass values. Al atoms ($M_{Al} = 27.0$ g/mol), are approximately two times lighter than the Fe and Ti ones. In consequence, the quantity of Al vapor is smaller, so the expansion of the ablated matter is stopped by the compressed surrounding air much closer to the sample surface than in case of Fe or Ti.

To resume, there are a lot of parameters, including target material physical properties that influence the process of laser ablation and plasma plume expansion. Finally, the most appropriate solution to examine the influence of target composition on the plasma plume expansion would be to compare the obtained results to a laser ablation model which would take into account all relevant physical properties of the materials, as well as experimental conditions.

E. Discussion

Impact of the laser beam on target surface induces melting and rapid evaporation of the target material. At a certain value of laser beam irradiance, initial gas breakdown occurs above the target surface, leading to a plasma plume forma-tion. This plasma plume absorbs a large amount of laser radiation, it gets heated and expands with a high velocity in the direction of the laser beam. In case of IR laser radiation, absorption of the laser beam energy by the plasma plume is carried out through the inverse bremsstrahlung process. Depending on the applied laser beam irradiance, different absorption waves may occur: laser-supported combustion wave, and laser-supported ablation wave.[43,44] In case of the laser supported ablation wave, laser radiation is absorbed within a thin front layer of the plasma, the plume expands with a supersonic velocity and drives a shock wave into the ambient gas. Across the shock wave, the ambient gas gets heated and ionized thus becoming a new thin front plasma layer being capable of absorbing laser radiation.

In case when plume expansion occurs in the ambient atmosphere, the influence of the ambient gas on plume expansion becomes more and more significant with the increase of the ambient pressure. Under our experimental conditions, at least three effects of the ambient gas may be expected:

(1) Along its axis of symmetry, the plume undergoes an acceleration, which can be described by the shock model given by Sedov[43]

$$R \propto (E_0/\rho_0) \, t^{2/5}. \tag{1}$$

This model describes the expansion of a spherical shock-wave formed due to the fast release of initial energy E_0 through a background gas of density ρ_0. One may notice that in our experiment the size of the laser spot is comparable to the plume size, questioning the applicability of the spherically symmetrical shock model. Still, one should keep in mind that the incident laser beam had a Gaussian intensity distribution, meaning that after being focused the beam delivered the greatest part of its energy to the center of the laser spot.

At later stages of its expansion, the plume slows down due to the drag resistance caused by the pressure of the ambient gas. So, the propagation of the plume front may be described by a drag model[28]

$$R = R_0[1 - \exp(-\beta \, t)], \tag{2}$$

where R_0 is the stopping distance of the plume and β is the slowing coefficient ($R_0\beta = v_0$ from shock model). This effect is supposed to be important under our experimental conditions. Here we point out that the exponential function fitting the experimental data for plume periphery length [see Fig. 8(b)] is in a good agreement with Eq. (2). In addition, fitting functions in Figs. 7(b) and 8(a) have the same form. The exponential functions given in Figs. 7(b) and 8 can be written in the following manner

$$R = R_0 \left(1 - \frac{a}{R_0} \exp(-\beta \, t) \right), \tag{3}$$

where the coefficient a/R_0 needs to be additionally introduced. It is obvious that these functions do not reach the origin (0,0). This, on the other hand, may be explained by the change of the plume expansion regime shortly after the end

of the laser pulse, somewhere between 5.1 and 10 ns. The period where the plume expansion is described by the shock model is much shorter than the period corresponding to the drag model. This is why the experimental data obtained in this work (for $t \geq 10$ ns) are well fitted by the exponential functions.

In addition, one may notice that the slope of the temporal evolution does not vary with the laser beam irradiance [Fig. 11(d)], indicating that the exponential coefficient β depends only on the target material. Once the exponential coefficient is determined, one can predict the plume expansion for any laser beam irradiance using the equation of shock model in conjunction with the drag model.

(2) Contrary to the plume expansion in the longitudinal direction, the radial expansion is not supported by the momentum of the initial laser energy deposition. This may explain why radial plume expansion velocity does not depend on laser beam irradiance [Fig. 11(c)], neither on target material [Fig. 12(c)]. In this case, the radial plume deceleration is mainly due to the pressure of the surrounding air.

(3) Fast expanding laser ablation plume penetrates the background gas and undergoes a deceleration due to the ambient pressure. This plume is characterized by a very low density, approximately 1000 times lower than the density of the ambient air. Under these conditions, the interface between the plasma and the ambient gas is known to be unstable and all perturbations seeded at this interface will be amplified. This is the so-called Rayleigh-Taylor instability (RT),[49,50] which grows in a linear regime proportionally to $(kg)^{1/2}$, where k is the wave number and g the interface acceleration. The initial perturbations may essentially come from the spatial laser beam intensity distribution. Thus, the wave number is related to the perturbation wavelength via $k = 2\pi/\lambda_{\mathrm{RT}}$, where λ_{RT} is approximately equal to the diameter of the laser spot, i.e., 1.72 mm. This may explain why plasma plume penetrates the ambient air with a spatial shape characterized by a spike on the axis (Fig. 2). Fourier decomposition also includes the 2nd and subsequent harmonics which may also grow in time, explaining the substructures observed in the plume. Let us now estimate the characteristic growing time of the perturbation, which may be expressed as the inverse of the growth rate. From Fig. 9 we can estimate the acceleration of the hot central region as $g = 1.15 \times 10^{10}\,\mathrm{m/s^2}$. Obviously, the acceleration of the low density interface is higher since its initial velocity is larger. Numerical simulations give a factor of 10 between the low density plasma plume and the hot core region at the end of the laser pulse (Sec. IV), but final asymptotic velocities should be comparable. In that case, the growth rate is equal to $\omega_{\mathrm{RT}} = 2 \times 10^7\,\mathrm{s^{-1}}$. It gives 50 ns characteristic growth time comparable to the characteristic time scale of the plume expansion. This may explain the peak formation, as well as the subsequent subharmoinc at longer times observed in Fig. 2. This explanation is confirmed by the fact that at lower laser beam irradiances, leading to a reduction of the plume expansion velocity, as well as of the Rayleigh – Taylor growth rate, the peak formation does not appear any more (Fig. 10).

(4) Plume issuing form the target into the ambient gas is similar to an underexpanded jet issuing suddenly from a
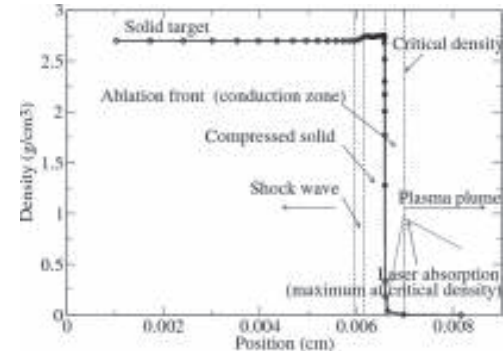
FIG. 13. Density as a function of the relative target position, obtained by 1D CHIC simulation at time $t = 1$ ns in aluminum. From left to right: shock wave propagating to the left, followed by the ablation front, i.e., ionization and conduction zone, and the plasma plume propagating to the right. Absorption of the laser radiation occurs in the plasma plume for densities lower than the critical density.

sonic nozzle into an ambient atmosphere, which reveals some vortical flow formation at the jet periphery.[51] This vortical flow is formed at the early stage of the jet expansion and it is shown that the gas involved into vortical motion has a subsonic velocity, while the jet core is supersonic. Moreover, it may induce a mixing of the ambient cold air with the plasma, which will enhance the plasma cooling at the plume periphery. This effect is clearly visible in the images recorded by the ICCD camera (see Fig. 2), but we cannot estimate the influence of the plasma-air mixing.

IV. ESTIMATES BY MODELS AND NUMERICAL SIMULATIONS

A. Estimates of ablation and plasma plume parameters

Let us now use some scaling laws to estimate parameters characterizing the plasma plume formed under our experimental conditions. At the very beginning of the laser pulse, during the first few tens of picoseconds or less, laser energy is absorbed within the skin depth of the treated material (less than 100 nm), which produces a sudden increase in temperature and pressure, and transforms this thin layer of solid matter into a plasma. Laser irradiance at the center of the laser beam increases up to its maximum of 16.32 GW/cm^2 at $t = 2$ ns. Since the laser beam has a Gaussian intensity distribution, the irradiance at the center of the laser beam was considered to be $I_0 = 16.32$ GW/cm^2 for the average irradiance value of $I_{\mathrm{av}} = 8.16$ GW/cm^2. In aluminum, skin depth may be evaluated as

$$d = c/2\omega\,k, \qquad (4)$$

where $c = 3 \times 10^8$ m/s, refractive index $k = 8.3$ and the laser frequency $\omega = 1.8 \times 10^{15}\,\mathrm{s^{-1}}$ (for $\lambda = 1064$ nm), which gives d = 10 nm. With a $c_s = 6$ km/s sound speed, we assume that the hydrodynamic process starts at a time larger than $t = d/c_s = 1.67$ ps. Assuming a constant laser power, no less

than $P = I_0/d = 1.632 \times 10^{16}$ W/cm^3 will be reached within the skin depth, which is higher than the aluminum Bulk modulus. This generates a shock wave in the target, followed by an ablation wave and an expansion wave, i.e., the plasma plume (Fig. 13). This plume is composed of low density hot temperature plasma, whose expansion is directed by the laser-supported ablation wave.

Quantities like shock wave, ablation wave and plasma plume velocities and densities may be estimated by scaling laws (see for instance Hughes[52] pp. 293–299). For instance, ablation front velocity is given by

$$v_{abl} = \sqrt{\frac{4}{(\gamma+1)}\left(1 - \frac{1}{\gamma_{pl}}\right)\frac{\rho_c}{\rho_s}\sqrt{\left(\frac{\gamma_{pl}+1}{\gamma_{pl}-1}\right)\frac{1}{2\rho_c^2}I^{2/3}}}, \quad (5)$$

plasma plume expansion velocity as

$$v_{plume} = \frac{2}{\gamma_{pl}-1}\sqrt[3]{\frac{\gamma_{pl}-1}{\gamma_{pl}+1}\frac{2I}{\rho_c}}, \quad (6)$$

and plasma temperature as

$$T_{pl} = \frac{M v_{plume}^2}{\gamma_{pl}R}, \quad (7)$$

where ρ_s is the density of the solid target material, ρ_c is the critical plasma density, and γ and γ_{pl} are the adiabatic ratios of the solid target and plasma, respectively. M is the molar mass of the target material, and R— the universal gas constant. I is the laser beam irradiance absorbed by the target material

$$I = \alpha_{mat}I_0, \quad (8)$$

where I_0 is the incident laser beam irradiance. Laser power absorbed per unit area of the laser beam cross section in a plasma depth l can be expressed as

$$I_a = I[1 - \exp(-a_\omega l)], \quad (9)$$

where a_ω is absorption coefficient of laser radiation (of frequency ω) through the inverse bremsstrahlung process. Assuming an optically thin plasma, i.e., $l \ll 1/a_\omega$, expression (9) can be approximated to

$$I_a \approx I a_\omega l. \quad (10)$$

From here, the mean laser radiation absorption rate per unit volume of plasma in the probed region is $I a_\omega$ (W/cm^3). The critical plasma density may be calculated as

TABLE I. Estimates of some ablation and plasma plume parameters using scaling laws. Calculations performed for the incident laser beam irradiance of $I_0 = 16.32$ GW/cm^2, corresponding to the average irradiance of $I_{av} = 8.16$ GW/cm^2.

Target material	ρ_c (g/cm^3)	T_{pl} (K)	v_{plume}(m/s)	v_{abl} (m/s)
Al (Z = 3)	0.01	1.85×10^6	3.1×10^4	1.8×10^3
Ti (Z = 2)	0.04	2.94×10^6	2.9×10^4	1.9×10^3
Fe (Z = 2)	0.05	2.67×10^6	2.7×10^4	1.3×10^3

$$\rho_c = \frac{m_i}{Z}\frac{m_e \varepsilon_0}{e^2}\omega^2, \quad (11)$$

where m_i is the ion mass, m_e – the electron mass, e – the elementary charge, ε_0 – the vacuum permittivity, ω – the laser frequency and Z – the effective charge of ions.

Estimates of these four parameters (ρ_c, v_{abl}, v_{plume}, T_{pl}) for our experimental conditions are presented in Table I. It can be observed that the estimated parameters depend on target material. Material properties that influence the values of these four parameters are: density of the solid target (ρ_s), laser radiation absorption coefficient (α_{mat}), effective charge of ions (Z), and molar mass (M).

Estimated plume velocity (v_{plume}) represents the expansion velocity of the entire laser ablation plume. As previously mentioned, cold zones of the plume, situated in front of the hot zones, may propagate with higher velocities. Hence, it is very possible that the cold zones propagate with velocities of the order of 10^4 m/s, while the hot zones expand with velocities of the order of 10^3 m/s, as measured by the imaging technique in this work.

The estimated values of plasma temperature and plasma plume expansion velocity for different materials are relatively similar. Ablation velocities of aluminum and titanium are larger than the one of iron. This means that more plasma will be generated in case of aluminum and titanium. Titanium is less conducting than aluminum. Hence, the thermal losses in titanium sample are expected to be lower, whereas a nuclei production rate is expected to be higher.

At this point of the study, scaling laws give no more than qualitative information. In the following section, we give results of CHIC numerical simulations, expected to finely reproduce plasma hydrodynamics, taking into account the ambient gas pressure.

B. Numerical simulations with code CHIC

A 2D hydrodynamic code CHIC (Code d'Hydrodynamique du CELIA) has been utilized to obtain some characteristic elements of the laser induced expanding plasma plume. CHIC[53] is a Lagrangian code developed at CELIA laboratory, and dedicated to inertial confinement fusion (ICF)
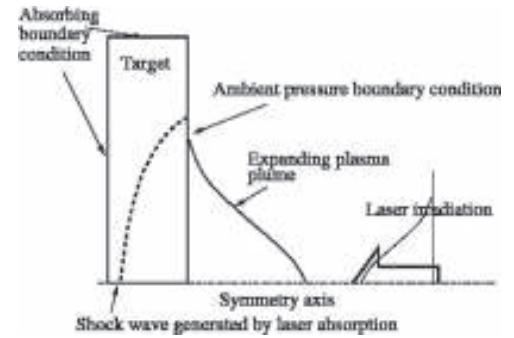
FIG. 14. Target model, boundary conditions and sketch of the shock wave and expanding plasma plume.

calculations. This code operates in 1D and 2D axially symmetric versions and it includes 3D ray tracing for laser beam propagation. The absorbed laser energy is controlled by calculating a collision frequency from electron−ion collision corrected to electron−phonon frequency at low temperature. Electron thermal transport is described by the classic Spitzer−Harm approximation, with flux limiter for high laser intensities. Equation of state is tabulated: SESAME[54] as well as BLF (Bushman−Lomonosov and Fortov)[55] tables can be read to account for both solid aluminum and plasma hydrodynamics. For aluminum, BLF table was used. For titanium and iron, tables SESAME S2962 and S2150 were used, respectively. It must be pointed out that these tables were not made for very low densities, such as those of the long time expanding plasmas.

Thomas−Fermi model was used to estimate the ionization. Special Arbitrary-Lagrangian−Eulerian scheme has been introduced in this code,[56] enabling a high precision remapping of both compressed and expanding plasma. Such
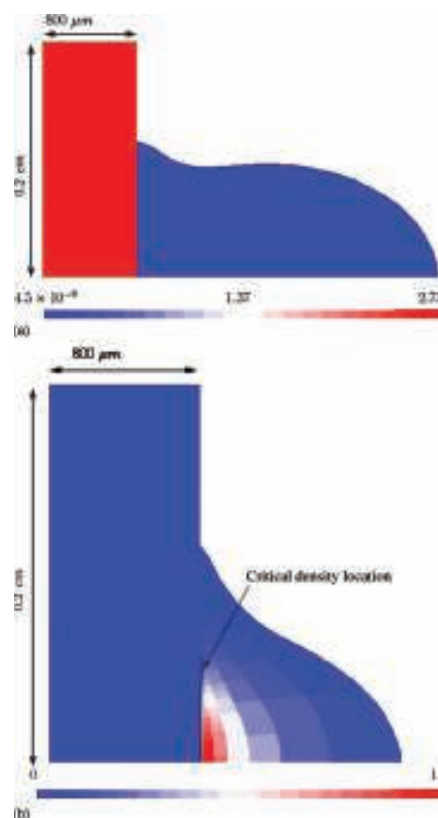
FIG. 15. (Color online) (a) Density contours (in g/cm^3) and (b) absorbed laser power contours characterizing laser ablation plume induced on the aluminum target at the instant $t = 10$ ns. Limit of the absorption region corresponds to the critical density location. Initial target dimensions are: 0.2 cm height and 800 μm thickness.

a simulation code offers the possibility to estimate the part of the absorbed laser energy within the target and the plasma, while the target undergoes a shock wave compression and deformation, followed by the process of plasma expansion in the ambient gas. CHIC enables one to calculate spatial distributions of electron and ion temperatures and densities, which can then be used to estimate the spectral power density of bremsstrahlung radiation emitted by the expanding plasma plume.

Target model utilized for CHIC simulations is presented in Fig. 14.

The target is 800 μm thin and 0.2 cm high with an axis of symmetry corresponding to the direction of the laser beam. Laser beam irradiance is described by a spatial Gaussian distribution of 860 μm width. Refraction was not taken into account. Mesh has been stretched in the absorption region with a 10 nm first cell thickness and a geometric expansion to cover the whole target thickness. Absorbing conditions have been applied to the rear and front surface of the target to limit the size of the domain, i.e., the computational costs. At the front surface, absorption of the laser radiation has been described by inverse bremsstrahlung process and the ambient pressure has been imposed. Contrary to 1D simulations, plasma plume expansion and the shock wave propagation in the target are expected to have a 2D geometry. Indeed, shock wave has to overcome the volumic strength of the matter and plasma plume expands from a central symmetry point in the ambient gas (see Sec. III E, shock model). This will have the effect of slowing down the radial expansion of the plasma plume periphery. In the meantime, the transverse velocity component will increase due to the ambient pressure, leading to enlarging the plasma plume and cooling down the plume periphery more rapidly than the central part of the plume.

Figure 15(a) shows a typical density distribution and Fig. 15(b) absorbed laser power distribution in the laser ablation plume induced on aluminum target at the instant $t = 10$ ns, calculated by CHIC code.

Figure 16 presents density, ionization degree, temperature and pressure contours that characterize laser ablation plume induced on aluminum target at the instant $t = 20$ ns, calculated by CHIC code. Expansion of the plume is adiabatic, quasi-isothermal. Density is low due to the fast plume expansion. Temperature contours show a lateral cooling down of the plume, leading to an emissivity decrease. Pressure maximum is due to the shock wave propagation in the solid target. The pressure is not sufficiently high to produce detectable radiative emission.

Data from Fig. 16 were used to compute the emitted radiation power, presented in Fig. 17. Spectral power density of bremsstrahlung radiation may be calculated as[57]

$$\xi_{br}^\lambda \approx \frac{32\pi\, e^6}{3c^2 m_e (4\pi\varepsilon_0)^3} \sqrt{\frac{2\pi}{3m_e k_B T_e}}\, g\, Z_i^2 N_e N_i \frac{1}{\lambda^2} \exp\left(-\frac{hc}{\lambda k_B T_e}\right)$$

$$(12)$$

where N_e and N_i represent electron and ion density respectively, T_e — electron temperature and Z_i — effective charge
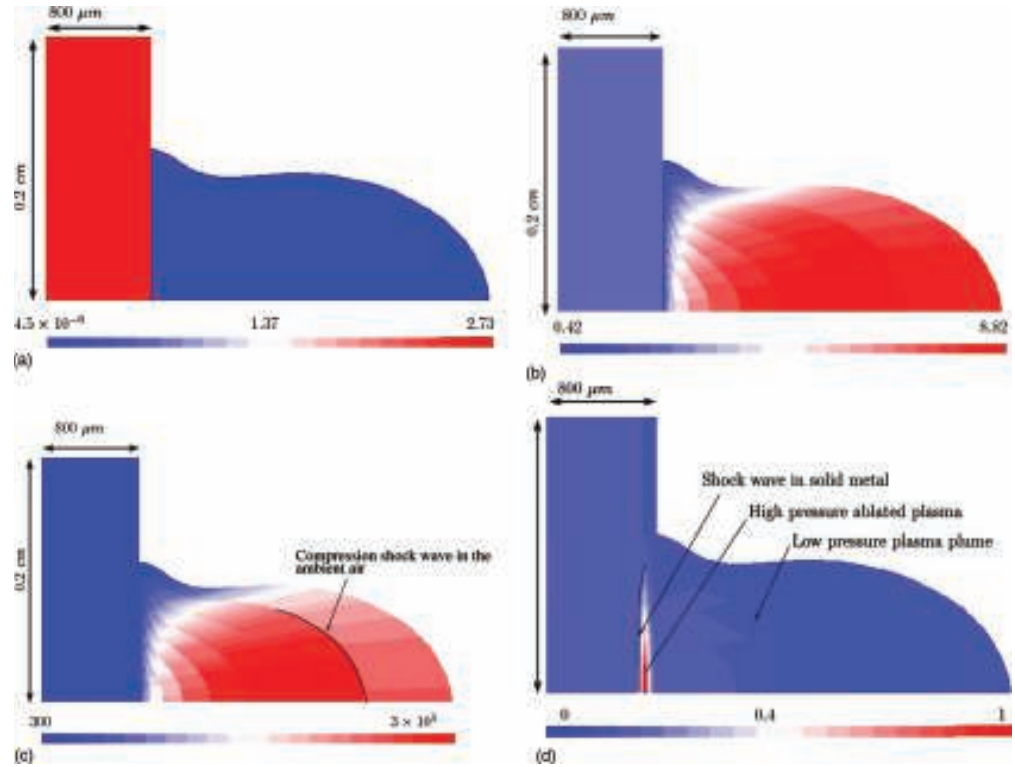
FIG. 16. (Color online) (a) Density (in g/cm^3), (b) ionization degree, (c) temperature (in K) and (d) pressure (in GPa) contours characterizing laser ablation plume induced on the aluminum target at the instant $t = 20$ ns, calculated by CHIC. It is shown that the plasma plume expands both radially and transversally. The region including hot and ionized plasma, as well as the absorption zone, is ejected to the right, i.e., in the direction of plasma plume expansion. Pressure maximum corresponds to the position of the shock wave in the target. The thermal flux, detected by the ICCD camera, corresponds to the hot and low density plasma.

of ions. λ is the wavelength of the laser radiation. g is the Gaunt factor, c — speed of light, h — Planck's constant and k_B — Boltzmann's constant. The emitted power density integrated over the radiation frequencies may be approximately expressed by[58]

$$P_{IB} \approx 1.69 \cdot 10^{-32} Z_i N_e^2 \sqrt{T_e(\text{eV})} \qquad (\text{W/cm}^3) \qquad (13)$$

The local value of the emitted radiation power may be calculated by multiplying Eq. (13) by a corresponding local volume element. Now, we can plot the contours of the emitted radiation power, normalized to the maximal radiation power value at $t = 20$ ns (Fig. 17). We estimate that the detection limit of the ICCD camera used in this work corresponds to about 10% of the maximal radiation power value detected.

From Fig. 17, it can be seen that the greatest part of radiation is emitted by a "tore tube" of the radius of 1 cm at $t = 20$ ns and 1.2 cm at $t = 30$ ns. By dividing the radiation power to the local cross section of the tore, we can obtain the intensity of the emitted radiation. This emitted radiation is higher on the periphery than toward the center of the tore, due

to a small increase in electron density at plasma periphery. By increasing the ambient pressure in the simulations, we have observed that electron density also increases. In the model, radiation which increases with N_e^2, is very sensitive to the ambient pressure. Here we can assume that a major part of the radiation is emitted from the hot zone periphery, which corresponds to the plume compression by the ambient air. This effect could also explain the discontinuity observed by the ICCD camera, i.e., the hot plasma core. From Fig. 17(b), it can be seen that the emitted radiation power reaches a threshold value (10% of the maximal value) at 1.5 cm (for $t = 30$ ns), which is slightly lower than the experimental result [$\approx$ 1.8 cm, Fig. 8(a)]. The lateral expansion is stopped when plasma pressure becomes equal to the atmospheric pressure.

Shortly after the end of the laser pulse, the velocity of the plume expansion in the longitudinal direction is much higher than the one in the lateral direction. This is why the electron density and temperature decrease much faster along the plume axis, leading to a quick reduction of the emitted radiation power along this direction (see Fig. 17). The effect of plume compression by the ambient air is not visible in the
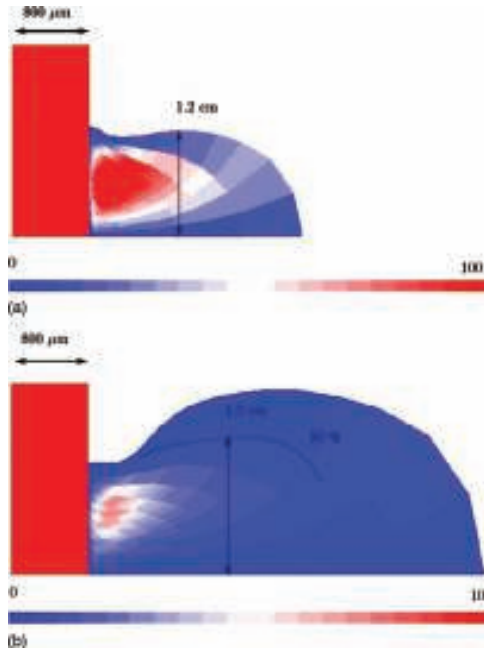
FIG. 17. (Color online) Cross-section distribution of the radiation power emitted from the aluminum plasma plume at (a) $t = 20$ ns and (b) $t = 30$ ns, normalized to the maximal radiation power value at $t = 20$ ns.

longitudinal direction (Fig. 17), due to much higher expansion velocities at $t = 20 - 30$ ns. Still, one can observe that the emitted radiation power reaches a threshold value (10% of the maximal value) at the distance of about 2.4 cm, which is slightly higher than the experimental result [$\approx$ 2 cm, Fig. 8(b)].
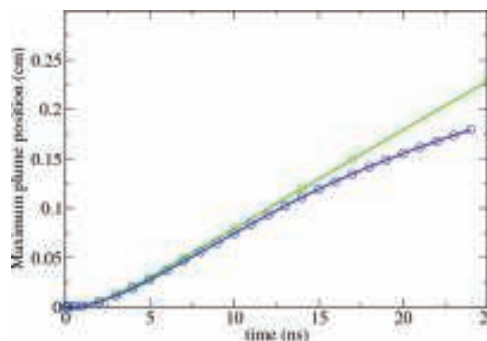
FIG. 18. (Color online) Temporal evolution of the plume expansion with (blue line and circle symbols) and without (green line and square symbols) the presence of the ambient gas. The effect of the ambient pressure is to slow down the edge of the expanding plasma plume. This slowing down of the plume expansion may be described by an exponential decrease, as predicted by a drag model, as well as observed from the experimental data.
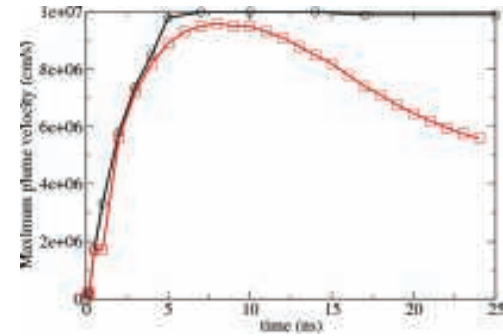
FIG. 19. (Color online) Temporal evolution of the plume maximal expansion velocity with (red line and square symbols) and without (black line and circle symbols) the presence of the ambient gas. Plasma plume which expands in the vacuum reaches a constant asymptotic velocity. When an ambient (atmospheric) pressure is imposed, plasma plume decelerates due to some drag effects.

Computations at later times are not presented, since hydrodynamic expansion would require a larger number of grid points with the expansion of the plume and because tabulated EOS have a reduced accuracy in the long time expanding plasma of a very small density.

However, from Fig. 17, one can clearly distinguish hot and cold zones of the ablation plume. In fact, numerical simulations describe the expansion of the entire ablation plume, while the ICCD camera detects only the hot zones of the ablation plume, whose expansion velocity is much lower than one of the plume edges. This explains the difference between the velocity values obtained from the experiment and by numerical simulation.
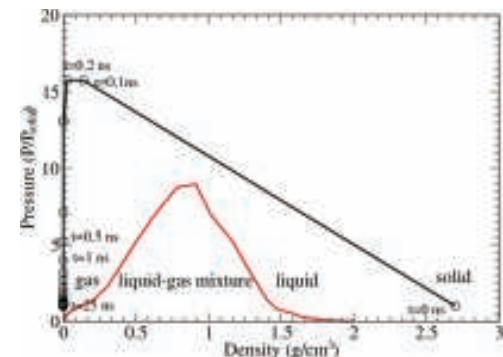
FIG. 20. (Color online) Thermodynamic path of the aluminum plasma plume expansion in the open air (circle) and saturation curve (in red). Initial conditions: standard conditions (2.7 g/cm^3, 1 bar). Then plasma begins heating and expansion process. At the beginning, up to $t = 0.2$ ns, heating is the dominant process. Then hydrodynamic expansion takes place and the pressure decreases. The edge of the plasma plume is no longer heated, since critical density is situated deeper inside the target and the plasma plume expands quasiadiabatically. At time $t = 25$ ns, the pressure-density conditions are close to the saturated state, i.e., the binodal curve. Nuclei, i.e., powders, may be produced from this moment on.

Temporal evolutions of the plume length and its maximal expansion velocity were calculated by CHIC in case of the presence and absence of the ambient gas (air). The presence of ambient air was taken into account using the half-Riemann problem to compute the pressure of the shocked air. The results, given for the first 25 ns of the plasma life, are shown in Figs. 18 and 19. From Fig. 19, it can be observed that in the absence of the ambient gas, the plume expands with a quasiconstant velocity, even after the end of the laser pulse. In case of presence of the ambient gas, plume expansion velocity decreases as soon as the laser pulse ends, which is due to the formation of a compression wave at the plume – air interface. The curve corresponding to the temporal evolution of the plume length in the presence of the ambient gas (Fig. 18, blue line) can be described by the function characterizing the drag model [Eq. (2)], i.e., an exponential decrease which looks very similar to the one obtained from the experimental results. In this case, we do not observe any Rayleigh−Taylor instability (see Sec. III E) due to the applied boundary condition for air, which is an approximation of ambient air − plasma plume interface.

In order to see what can be expected from numerical simulations, we give Fig. 20 presenting the thermodynamic path of the aluminum plasma plume expansion in the open air. This curve is superimposed to the saturation, i.e., binodal curve in a pressure-density diagram. The thermodynamic path shows that the absorbed laser energy is sufficient to obtain hot and high pressure plasma in a time shorter than a nanosecond. The plume expands into the ambient air, characterized by a much lower pressure, leading to a pressure decrease at the front of the plasma plume. As a consequence, the front part of the plume does not absorb laser radiation any more. At time $t = 25$ ns, thermodynamic state is close to the one corresponding to the binodal curve. Later in time, we see that the plasma expands producing a liquid − gas mixture. According to Lescoute,[26] the thermodynamic state will not be in thermal equilibrium due to the fast expansion, which is a favorable condition for nuclei formation, ones the binodal curve has been crossed.

The fast photography results presented in this article offer the possibility to evaluate the size of the plasma plume region where the nuclei are most likely to be produced. By coupling these results with the scaling laws or numerical simulation data, one should be able to complete this diagnostics and determine at which moment of the plume expansion the nuclei will be produced.

V. CONCLUSION

In this work, structure and dynamics of the plasma plume induced by the impact of a nanosecond laser beam on metallic samples in the open air has been investigated using fast photography technique and numerical simulations.

Detailed analysis of the spatio-temporal evolution of the plasma plume at the early stage of its expansion has been performed. One should keep in mind that the images recorded by the ICCD camera in this work correspond to the hot zones of the laser ablation plume. The structure of the plasma plume has been observed. Two plume regions — *plume core* and

plume periphery — have been distinguished. Temporal evolutions of the plume core and periphery dimensions have been examined and their expansion velocities have been determined. Furthermore, it has been confirmed that laser beam irradiance, as well as the target material significantly influence the plasma plume expansion. The study of the plume expansion by fast photography technique enables us to determine the location of hot and dense emissive zones of the ablation plume, where the formation of nanoparticles will occur.

Experimental data have been cross-checked using the hydro-code CHIC and some scaling laws. Some quantities like plasma plume expansion velocity and plasma thermodynamic path have been computed as a function of time. These modeling results give additional information to the ones obtained from the experimental study. These data are only macroscopic, like characteristic size of plasma plume, position of the hot and low density region where nuclei are expected to begin their growth. The microscopic information obtained with numerical simulations may allow one, for instance, to place the diagnostics more finely and to have a better insight into the details of the expanding plume.

Detailed studies of plasma plume expansion are very important for a better understanding of the complex assembly of physical processes occurring at and above the sample surface during laser − matter interaction. This is necessary for a further development of laser ablation based technologies. Results obtained from detailed analyses of plasma plume dynamics can be useful for verification and further development of laser induced plasma models. In addition, the study of the influence that different parameters, like laser beam irradiance or target composition, have on plume dynamics may contribute to a better comprehension of the laser ablation process, including debris and particle formations in the expanding plasma plume. These latter studies have also useful applications for chamber dimensioning in the context of inertial fusion, as well as magnetic fusion reactors.

ACKNOWLEDGMENTS

[1]G. Dumitru, B. Luscher, M. Krack, S. Bruneau, J. Hermann, and Y. Gerbig, Int. J. Refract. Met. Hard Mater. **23**, 278 (2005).
[2]A. Kr. Dubey and V. Yadava, J. Mater. Process. Technol. **195** 15 (2008).
[3]I. Etsion, J. Tribol. **127**, 248 (2005).
[4]J. Jandeleit, A. Horn, R. Weichenhain, E. W. Kreutz, and R. Poprawe, Appl. Surf. Sci. **127–129**, 885 (1998).
[5]C. Molpeceres, S. Lauzurica, J. L. Ocana, J. J. Gandia, L. Urbina, and J. Carabe, J. Micromech. Microeng. **15**, 1271 (2005).
[6]E. V. Bordatchev, Y. Lai, and S. K. Nikumb, J. Phys.: Conf. Ser. **59**, 700 (2007).
[7]V. Zorba, I. Alexandrou, I. Zergioti, A. Manousaki, C. Ducati, A. Neumeister, C. Fotakis, and G. A. J. Amaratunga, Thin Solid Films **453–454**, 492 (2004).
[8]P. R. Willmott and J. R. Huber, Rev. Mod. Phys. **72**, 315 (2000).
[9]C. Cibert, H. Hidalgo, C. Champeaux, P. Tristant, C. Tixier, J. Desmaison, and A. Catherinot, Thin Solid Films **516**, 1290 (2008).
[10]A. Buzas, L. Egerhazi, and Zs. Geretovszky, J. Phys. D **41**, 085205 (2008).

[11] T. Yamamoto, K. Kikunaga, K. Obara, N. Terada, N. Kikuchi, T. Tanaka, K. Tokiwa, T. Watanabe, A. Sundaresan, and Shipra, Supercond. Sci. Technol. **20**, S461 (2007).

[12] R. W. Eason, T. C. May-Smith, C. Grivas, M. S. B. Darby, D. P. Shepherd, and R. Gazia, Appl. Surf. Sci. **255**, 5199 (2009).

[13] M. F. Becker, J. R. Brock, H. Cai, D. E. Henneke, J. W. Keto, J. Lee, W. T. Nichols, and H. D. Glicksman, Nanostruct. Mater. **10**, 853 (1998).

[14] S. Vijayalakshmi, M. A. George, J. Sturmann, and H. Grebel, Appl. Surf. Sci. **127–129**, 378 (1998).

[15] T. Donnelly, S. Krishnamurthy, K. Carney, N. McEvoy, and J. G. Lunney, Appl. Surf. Sci. **254**, 1303 (2007).

[16] L. J. Radziemski, Spectrochim. Acta, Part B **57**, 1109 (2002).

[17] R. Fantoni, L. Caneve, F. Colao, L. Fornarini, V. Lazic, and V. Spizzichino, Spectrochim. Acta, Part B **63**, 1097 (2008).

[18] J. S. Becker, Spectrochim. Acta, Part B **57**, 1805 (2002).

[19] A. Vogel and V. Venugopalan, Chem. Rev. **103**, 577 (2003).

[20] J. Colombelli, E. G. Reynaud, and E. H. K. Stelzer, Med. Laser Appl. **20**, 217 (2005).

[21] N. Nwaejike, P. D. Srodon, and C. Kyriakides, Ann. Vasc. Surg. **23**, 39 (2009).

[22] J. Serbin, T. Bauer, C. Fallnich, A. Kasenbacher, and W. H. Arnold, Appl. Surf. Sci. **197–198**, 737 (2002).

[23] L. Lavisse, M. C. Sahour, J.-M. Jouvard, G. Pillon, M. C. Marco de Lucas, S. Bourgeois, and D. Grevey, Appl. Surf. Sci. **255**, 5515 (2009).

[24] I. Shupyk, L. Lavisse, J.-M. Jouvard, M. C. Marco de Lucas, S. Bourgeois, F. Herbst, J.-Y. Piquemal, F. Bozon-Verduraz, and M. Pilloz, Appl. Surf. Sci. **255**, 5574 (2009).

[25] E. Lescoute, L. Hallo, B. Chimier, D. Hébert, V. T. Tikhonchuk, C. Stenz, J.-M. Chevalier, J.-L. Rullier, and S. Palmier, Eur. Phys. J. Spec. Top. **175**, 159 (2009).

[26] E. Lescoute, L. Hallo, D. Hébert, B. Etchessahar, V. T. Tikhonchuk, J. M. Chevalier, and P. CombisPhys. Plasmas **15**, 063507 (2008).

[27] S. S. Harilal, C. V. Bindhu, M. S. Tillack, F. Najmabadi, and A. C. Gaeris, J. Phys. D **35**, 2935 (2002).

[28] S. S. Harilal, C. V. Bindhu, M. S. Tillack, F. Najmabadi, and A. C. Gaeris, J. Appl. Phys. **93**, 2380 (2003).

[29] S. Gurlui, M. Agop, P. Nica, M. Ziskind, and C. Focsa, Phys. Rev. E **78**, 026405 (2008).

[30] S. Amoruso, A. Sambri, and X. Wang, Appl. Surf. Sci. **253**, 7696 (2007).

[31] O. Barthelemy, J. Margot, and M. Chaker, IEEE Trans. Plasma Sci. **33**, 476 (2005).

[32] B. Wu, Y. C. Shin, H. Pakhal, N. M. Laurendeau, and R. P. Lucht, Phys. Rev. E **76**, 026405 (2007).

[33] J. S. Cowpe, J. S. Astin, R. D. Pilkington, and A. E. Hill, Spectrochim. Acta, Part B **63**, 1066 (2008).

[34] R. Viskup, B. Praher, T. Stehrer, J. Jasik, H. Wolfmeir, E. Arenholz, J. D. Pedarnig, and J. Heitz, Appl. Surf. Sci. **255**, 5215 (2009).

[35] L. Lavisse, J. M. Jouvard, J. P. Gallien, P. Berger, D. Grevey, and Ph. Naudy, Appl. Surf. Sci. **254**, 916 (2007).

[36] M. Hauer, D. J. Funk, T. Lippert, and A. Wokaun, Opt. Lasers Eng. **43**, 545 (2005).

[37] H. Schittenhelm, G. Callies, P. Berger, and H. Hugel, Appl. Surf. Sci. **127–129**, 922 (1998).

[38] A. De Giacomo, M. Dell'Aglio, R. Gaudiuso, G. Cristoforetti, S. Legnaioli, V. Palleschi, and E. Tognoni, Spectrochim. Acta Part B **63**, 980 (2008).

[39] O. Barthelemy, J. Margot, M. Chaker, M. Sabsabi, F. Vidal, T. W. Johnston, S. Laville, and B. Le Drogoff, Spectrochim. Acta, Part B **60**, 905 (2005).

[40] X. Wang and B. Man, J. Korean Phys. Soc. **32**, 373 (1998).

[41] J. A. Aguilera and C. Aragon, Appl. Surf. Sci. **197–198**, 273 (2002).

[42] S. Conesa, S. Palanco, and J. J. Laserna, Spectrochim. Acta, Part B **59**, 1395 (2004).

[43] Ya. B. Zel'dovich and Yu. P. Raizer, *Physics of Shock Waves and High-Temperature Hydrodynamic Phenomena*, 2nd ed. (Dover, New York, 2002), pp. 343–348.

[44] R. G. Root, *Laser-Induced Plasmas and Applications*, edited by L. J. Radziemski and D. A. Cremers (Marcel Dekker, New York, 1989), pp. 69–103.

[45] R. C. Weast, editor, *CRC Handbook of Chemistry and Physics*, (CRC Press, Boca Raton, FL, 1989).

[46] J. R. Davis, editor, *ASM Specialty Handbook: Aluminum and Aluminum Alloys* (ASM International, Materials Park, 1993).

[47] J. R. Davis, editor, *ASM Specialty Handbook: Titanium and Titanium Alloys* (ASM International, Materials Park, 1993).

[48] T. Iida and R. I. L. Guthrie, *The Physical Properties of Liquid Metals* (Clarendon, Oxford, 1988).

[49] L. Rayleigh, Proc. London Math. Soc. **14**, 170 (1883).

[50] R. P. Drake and P. A. Keiter, Phys. Plasmas **9**, 382 (2002).

[51] A. V. Bulgakov and N. M. Bulgakova, J. Phys. D: Appl. Phys. **31**, 693 (1998).

[52] T. P. Hughes, *Plasma and Laser Light* (Adam Hilger, London, 1975).

[53] P.-H. Maire, R. Abgrall, J. Breil, and J. Ovadia, SIAM J. Sci. Comput. **29**, 1781 (2007).

[54] C. Boettger, Tech. Rep. LA-12841, Los Alamos Technical Report No. LA-12841, 1994.

[55] P. R. Levashov and K. V. Kishchenko, Shock, Compression of Condensed Matter, AIP Conf. Proc. **955**, 59 (2007).

[56] P.-H. Maire, J. Breil, and S. Galera, Int. J. Numer. Methods Fluids **56**, 1161 (2008).

[57] I. H. Hutchinson, *Principles of Plasma Diagnostics* (Cambridge University Press, Cambridge, 2002).

[58] S. Gladstone and R. H. Lowberg, *Controlled Thermonuclear Reactions* (Van Nostrand, New York, 1960), Chap 2.